Keratin Cortex Stabilizes Cells and Cell-Cell Contacts at High Strains

Ruth Meyer,[1] Ulla Unkelbach,[2] Parul Jain,[3] Ulrike Rölleke,[1] Nicole Schwarz,[4] Amaury Perez-Tirado,[2] Anna V. Schepers,[1,5] Claudia Geisler,[3] Andreas Janshoff,[2,5,6,*] and Sarah Köster[1,5,6,†]

[1]*Institute for X-Ray Physics, University of Göttingen, Göttingen, Germany*
[2]*Institute of Physical Chemistry, University of Göttingen, Göttingen, Germany*
[3]*Department of Optical Nanoscopy, Institute for Nanophotonics Göttingen e.V., Göttingen, Germany*
[4]*Institute of Molecular and Cellular Anatomy, RWTH Aachen University, Aachen, Germany*
[5]*Max Planck School "Matter to Life," University of Göttingen, Göttingen, Germany*
[6]*Cluster of Excellence "Multiscale Bioimaging: from Molecular Machines to Networks of Excitable Cells" (MBExC), University of Göttingen, Göttingen, Germany*

(Received 30 August 2025; accepted 2 March 2026; published 31 March 2026)

The eukaryotic cytoskeleton consists of three filament types: actin filaments, microtubules, and intermediate filaments (IFs). IF proteins are expressed in a cell-type-specific manner, and keratins are found in epithelial cells. In certain cell types, keratin forms a layer close to the membrane which may be referred to as an "IF-cortex." It is hypothesized that this IF-cortex arranges with radial bundles in a "rim-and-spokes" structure in epithelia. Based on this hypothesis, IFs and actin filaments might add complementary mechanical properties to the cortex. It was previously shown that single IFs *in vitro* remain undamaged at high strains and display a nonlinear stretching behavior. We now ask whether this unique force-extension behavior of single IFs is also relevant in the context of a filament network within a cell. We show that keratin-deficient (KO) Madin-Darby canine kidney II cells readily form two-dimensional (2D) cell layers and 3D cysts and withstand high equibiaxial strains. High-resolution imaging using STED microscopy reveals altered actin cortex structures in KO cells, presumably in response to the missing keratin. We investigate the influence of the equibiaxial strain on the viscoelastic properties of wild-type (WT) and KO cells using atomic force microscopy. We find that the KO cells exhibit a higher prestress than the WT cells, likely due to the change of the cortical structure. Interestingly, both the prestress and the fluidity of the KO cells are altered already at intermediate strains, whereas the WT cells show a response only at high strain. Upon stretching, the WT cysts retain their intraluminal fluid, i.e., they possess tight cell-cell contacts, whereas a part of the KO cysts release the fluid due to deficient cell-cell contacts. The compressibility modulus is analyzed in a spatially resolved manner and we find this modulus to be increased at the cell rim, compared to the inside region, due to the geometry of the cell layer. Our results indicate that KO cells remodel their actin cytoskeleton to maintain function, but nevertheless the whole tissue is very sensitive to external strain. The intricate interplay between the actin and keratin cortices in WT cells preserves their mechanical state and the cell layer stability.

DOI: 10.1103/s24m-n8wc

I. INTRODUCTION

Cells in certain types of tissues permanently experience forces, caused by, for example, fluid flow and active contraction generated by neighboring cells or during peristaltic movement [1,2]. The cell can cope with these forces due to its cytoskeleton [1], a biopolymer network of three types of filamentous proteins—actin filaments, microtubules and intermediate filaments (IFs) [3]—along with passive cross-linkers and active motor proteins. Interestingly, each type of filament contributes unique mechanical and dynamic properties and together they organize into complex networks providing the cell with distinct mechanical properties and enabling the cell to flexibly adapt to mechanical requirements [3]. Of the three filament types, actin is considered to be the most relevant for cell mechanics [4], while microtubules contribute only little [4,5]. The importance of actin for cell mechanics and morphogenesis is reflected in the so-called cortex, a dense, contractile network found just underneath the plasma membrane [6].

In contrast to actin and tubulin, IF proteins are expressed in a cell-type-specific manner, each providing their own unique properties to the cell [7]. Specifically, epithelial cells express the IF protein keratin [8]. In certain cell types, such as Madin-Darby canine kidney (MDCK) cells [9], murine trophectoderm cells or murine enterocytes [10], the IF network forms a "rim" close to the cell membrane, just below the actin cortex and may hence also be referred to as an "IF-cortex." The cortex interconnects the desmosomes in a circumferential network organized in parallel to the plasma membrane and

*Contact author: andreas.janshoff@chemie.uni-goettingen.de
†Contact author: sarah.koester@uni-goettingen.de

is hypothesized to be part of a rim-and-spokes arrangement [9]. Furthermore, it has been shown that cells exhibit different mechanical properties in different regions of the cell [11–13], which raises the question of whether the rim-and-spokes arrangement contributes additional mechanical features to the properties of the cell, depending on the region.

In vitro rheology experiments on networks of actin, microtubules, and IFs show that actin and microtubules rupture at comparatively low forces, while IFs are highly extensible and remain undamaged at high strains [14–17]. This network extensibility found for IFs is also reflected on the single filament level: Vimentin IFs can be extended up to at least 4.5-fold their original length [18] and similarly high values were found for keratin, desmin, and neurofilaments [19–21]. Additionally, IFs are referred to as the "safety belt" of the cell as they are easily extensible at slow strain rates but stiffen when stretched fast [18,22–25]. Hence, a "two-layered" cortex in the cells made of mechanically highly distinct filament types, actin and IFs, could potentially lead to interesting properties of the cell when exposed to high forces. Moreover, it has been shown that vimentin IFs stiffen under compression, both in cells and *in vitro* [26] and it is not unlikely that a similar phenomenon may exist for keratin. These results from studies on IF networks and single filaments reveal two interesting features of this biomaterial: (i) They are more extensible than actin filaments that rupture at low strains and (ii) they display a distinctly nonlinear stress-strain behavior. At low strains, IFs behave linearly, at strains above 10% to 20%, they display a plateau regime in which little force is needed to extend the filament further, and at high strains they stiffen [18]. Thus, the plateau in the stress-strain behavior coincides with a strain regime where actin is already fluidized [27] and the question arises of whether the keratin is able to protect the cell from damage. To answer this question, cells may be strained by mechanical stretching [28] and, indeed, such cell stretchers, where cells are seeded on elastic membranes that are being stretched either uniaxially [25,29–32] or (equi)biaxially [33–35], have been developed and applied. Alternative methods for stretching of cells exist, such as suspended cell monolayers [2,36], single cells between two plates [37], or cell "domes" [38]. These studies revealed a strain-stiffening of the cells already at 14% linear strain [34]. The actin network reorganizes along the stretching direction [27,29,31,32], while IFs reorganize as well but are much more extensible and stabilize the cell [25,36].

Despite these insightful studies, which clearly point to an important role of IFs in cell mechanics, it remains unclear whether and to which extent the unique stress-strain behavior of individual IFs is relevant in the cell. We hypothesize that especially at high strains, the high extensibility and the nonlinear stress-strain behavior of IFs influence the viscoelastic properties of the cells. To investigate this hypothesis on MDCK II epithelial cells, we employ an equibiaxial cell-stretcher, compatible with both atomic force microscopy (AFM) and light microscopy. As a complementary approach, we present a method to stretch three-dimensional (3D) MDCK II tissue to high strains through microinjection, enabling us to stretch cell layers without the need of an elastic substrate as well as accelerating the stretching process in comparison to the equibiaxial cell stretcher to investigate the safety belt mechanism, i.e., the loading rate dependence of IF mechanics. We study the influence of the keratin network on cell mechanics by conducting AFM force spectroscopy on equibiaxially stretched wild-type (WT) and keratin knockout (KO) cells. By applying a suitable viscoelastic model to our data, we obtain three viscoelastic parameters, i.e., the prestress, fluidity, and area compressibility modulus. We perform complementary experiments by stretching 3D cell tissue, so-called cysts, through oil injection. We find that the prestress σ_0 is increased in keratin-deficient cells, possibly due to remodeling of the actin cortex in response to the missing keratin layer. Interestingly, the fluidity value β and the prestress σ_0 of the KO cells respond to intermediate strains, whereas for the WT cells they respond only for high strains. For the 3D cysts we observe that when grown from KO cells, a large fraction releases the intraluminal fluid upon stretching, which is not the case for cysts grown from WT cells, altogether pointing at a complex interplay between the actin and the keratin cortices in MDCK cells, with consequences for cell mechanics also on the tissue level. Furthermore, we distinguish between the cell edge and interior in a spatially resolved manner and find that the apparent compressibility modulus $\widetilde{K}_A$ is increased at the cell rim compared to the inside region, likely as a consequence of the "bricklike" geometry of the cell layers. Together with high-resolution imaging of the actin cortex, our findings suggest that in KO cells the actin structures are altered in response to the missing keratin network so as to maintain the mechanical properties, but only the combination of actin and keratin guarantees cell integrity under strain.

II. RESULTS AND DISCUSSION

A. Keratin KO cells withstand equibiaxial strain

To investigate cells under strain, we design a cell stretcher [Fig. 1(a)] that pulls on an elastic polydimethylsiloxane (PDMS) membrane (cyan) equibiaxially by turning the six arms (light gray) outwards in an "irislike" motion (small pink arrows). We first thoroughly characterize the stretcher by adding a layer of fluorescent beads as fiducial markers to the membrane (Fig. S1(a) in the Supplemental Material [39]) and by imaging the beads at different motor positions (mp) of the stretcher. We analyze the displacement of the beads by registering the images and thus obtain the elongation of the membrane Δl between two motor positions of the stretcher, which we use to calculate the strain in x and y direction as

$$\varepsilon_i = \frac{\Delta l_i}{l_i} \quad \text{with} \quad i = x, y \tag{1}$$

with the initial length l_i.

Figure 1(b) shows the linear strain ε_i in x and y direction against the applied steps of the motor (mp) ($N = 21$ independent experiments). The solid lines represent the average from all experiments in x (black) and y (pink) direction. The shaded areas present the standard deviations. We find the same linear strain in x and in y direction, confirming that the stretcher indeed pulls uniformly in both directions. This is in contrast to uniaxial strain, where the elastic membrane and therefore the cell sample is stretched in one direction and compressed perpendicularly to the stretching direction according to the Poisson's ratio [40]. A good measure to quantify the degree of

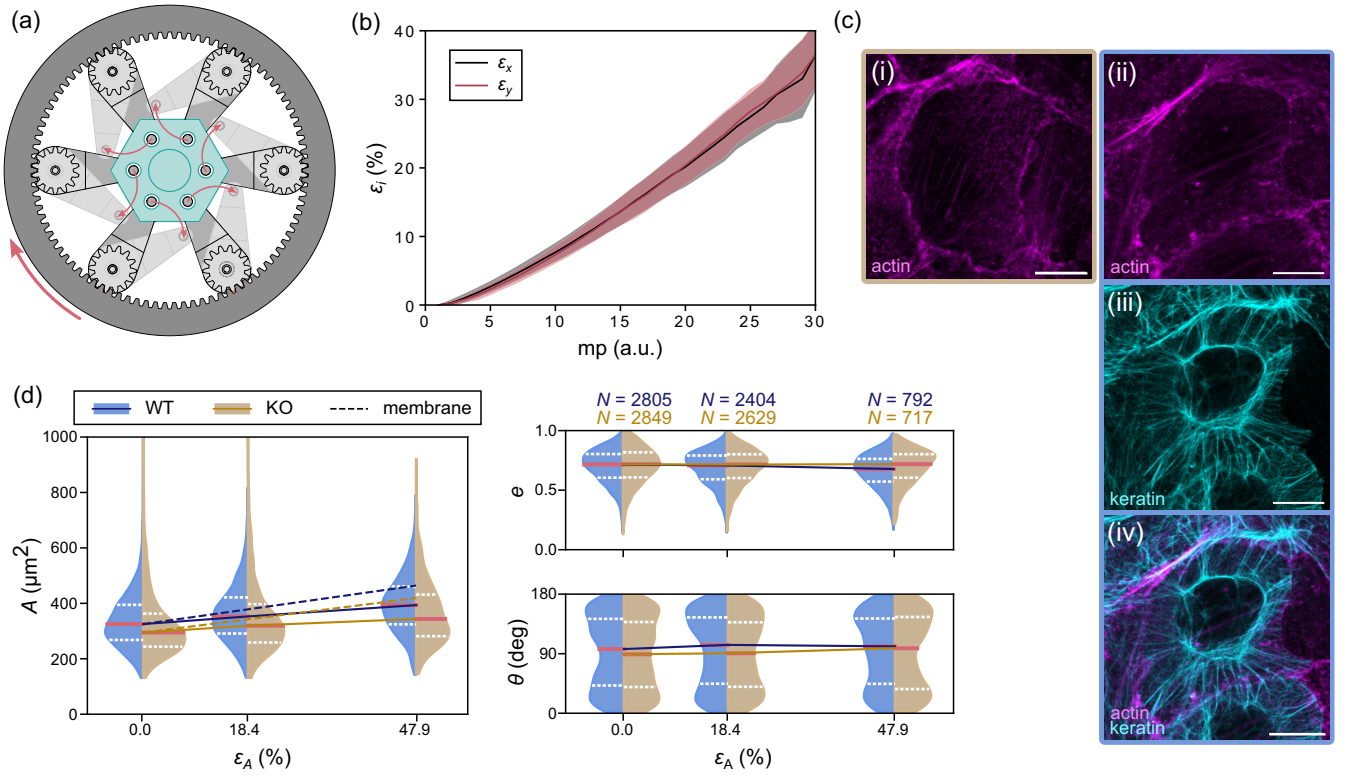

FIG. 1. Experimental setup and characterization of the cell stretcher. (a) Schematic of the equibiaxial stretcher. A PDMS device (cyan) is attached to the six arms of the stretcher (light gray). The motor rotates the outer internal gear ring (dark gray, large pink arrow), which then moves the arms outwards (small pink arrows). (b) Averaged linear strain ε_i (x and y directions) of the PDMS membrane, calculated from the beads embedded in the membrane, plotted against the motor steps (mp); the shaded areas show the standard deviation. (c) Examples of confocal microscopy images of the cell lines used in the study. (i) Fixed, unstrained MDCK II K8 KO cells with phalloidin-stained actin (magenta), referred to as KO. [(ii)–(iv)] Fixed, unstrained MDCK II WT cells transfected with lifeact actin tagged with mCherry, here additionally stained with phalloidin [magenta (ii)], and keratin 8 tagged with EGFP [cyan (iii)], referred to as WT [composite (iv)]. Scale bars correspond to 10 µm. (d) Area A (left), eccentricity e, and orientation θ (right) of the WT (blue) and KO (yellow) cells plotted against the area strain ε_A. The violin plots show the distribution of the results for each individual cell with the median (solid pink lines) and upper and lower quartiles (dashed white lines). Medians are connected using solid lines. Dashed lines show the theoretically expected area of the cells calculated from the characterization of the membrane. The numbers of cells N are provided in the figure and correspond to all data.

stretching is therefore the area strain ε_A. The two-dimensional area strain can be described as

$$\varepsilon_A = \frac{A_{\text{new}} - A_0}{A_0}$$

and hence [41]

$$\varepsilon_A = \frac{x_{\text{new}} y_{\text{new}} - x_0 y_0}{x_0 y_0}$$

for the area $A = x \cdot y$. Substituting x_{new} and y_{new} by $x_0 + \Delta x$ and $y_0 + \Delta y$, respectively, we obtain

$$\varepsilon_A = \frac{(x_0 + \Delta x)(y_0 + \Delta y) - x_0 y_0}{x_0 y_0} = \frac{\Delta x}{x_0} + \frac{\Delta y}{y_0} + \frac{\Delta x}{x_0} \cdot \frac{\Delta y}{y_0}.$$

Using the definition of linear strain [Eq. (1)] yields

$$\varepsilon_A = \varepsilon_x + \varepsilon_y + \varepsilon_x \cdot \varepsilon_y.$$

Finally, for equibiaxial strain $\varepsilon_x = \varepsilon_y$, the area strain can be written as

$$\varepsilon_A = 2\varepsilon_x + \varepsilon_x^2. \tag{2}$$

For our experiments, we use epithelial MDCK II cells which naturally express keratin 8/18 in a rim-and-spokes arrangement [9]. For visualization of the keratin and actin networks, the cells are transfected with keratin 8 tagged with EGFP and lifeact actin tagged with mCherry [Figs. 1(cii)–1(civ)]. In the following, we will refer to these cells as WT cells. Additionally, to investigate the influence of the keratin network on the mechanical properties, we use MDCK II K8 KO cells. Immunostaining against keratins K4, K5, K6, K7, K8, K10, K14, K15, K16, and K19 and vimentin confirms that in the KO cells none of the tested keratins is present and vimentin is expressed at the same level as in WT cells (Fig. S2 in the Supplemental Material [39]).

The basal side of the cells is tightly adherent to the PDMS membrane and is thus expected to follow its strain. As the cells are grown on the PDMS membrane in a confluent monolayer and are connected via desmosomes, adherens junctions and tight junctions, for geometry reasons, in first approximation we expect the basal side to experience the same strain as well. To confirm the stretching of the cells, we image them with phase contrast microscopy at increasing mp of the stretcher (N = 10–11 independent experiments). The images are

segmented to determine the area A, orientation θ, and eccentricity e (Eq. (A1) and Figs. S3(d) and S3(e) Supplemental Material [39]).

Figure 1(d) shows the results of this analysis for increasing area strains ε_A as violin plots. The WT cells are displayed in blue and the KO cells in yellow. As a guide to the eye, the medians are connected by solid lines in the respective colors. Additionally, we show the theoretically expected value for the area from Eq. (2), considering a perfect and complete transfer of the strain from the membrane to the cells and using the median from each cell line at 0% strain as the starting value (dashed lines).

We find the KO cells to be smaller than the WT cells, as previously also observed for keratin 8 knockout hepatocytes [42]. Additionally, we observe an increase in cell size with increasing strain for both cell lines. The increase is lower than expected from the applied strain even though the cell layer remains intact and no holes in the cell sheet appear in the field of view. This deviation from the theoretical area values can have multiple reasons. The elastic membrane is coated with laminin to enhance cell adhesion. This attachment of the cells to the coating and the coating to the membrane can change and be disrupted during stretching leading to a lower strain transmission or an uneven strain distribution [34,35,43,44]. Furthermore, it has been shown that for treatment of the cells with latrunculin, hence weakening the focal adhesions through the inhibition of actin polymerization, the cell strain decreases considerably, proving the relevance of a good adhesion of the cell to the surface [34]. Additionally, the cell body is mechanically inhomogeneous, which can also lead to a reduced strain transmission on the cells [44]. As expected, the orientation and the eccentricity of the cells do not change with increasing strain; see Fig. 1(d), right, supporting the notion of equibiaxial strain.

With this cell stretcher design, we are able to stretch the elastic membrane up to a linear strain of 38% which translates to an area strain ε_A of 90% [Eq. (2)] and is higher than for other equibiaxial cell stretchers [28,33–35]. Here we stop stretching the elastic membrane at an area strain of 48% to ensure long-term measurements without risking yielding of the PDMS membrane. Additionally, we choose an intermediate strain approximately halfway between the maximum chosen strain and the relaxed position. Although the applied strain does not fully transfer to the cells, we are able to stretch both cell lines equibiaxially to an area increase of up to 23%. In the following, the area strain ε_A refers to the strain applied by the stretcher to the PDMS device. Our results show that even without a keratin network, the cells are well able to resist the equibiaxial strain.

B. The keratin cortex protects the cells at intermediate strains

Based on previous studies that show stiffening of individual IFs at strains beyond 10 to 20% [18], the question arises of whether the mechanical properties of the WT and KO cells differ under strain. Hence, we perform force mapping, i.e., combined AFM topography imaging with force spectroscopy measurements of the cell monolayers on PDMS membranes. Our stretcher is designed to fit on the stage of an AFM (Nanowizard 4, Bruker Nano GmbH). This setup enables simultaneous inverse light microscopy and AFM measurements [Fig. 2(a)]. Figure 2(b) (left) shows a typical topography image of a confluent cell monolayer, where the colors display the height differences within the sample from the lowest height (0 μm, dark blue) to the highest point (here: 2.68 μm, white). Note that this height difference is measured on top of the cell layer and not from the bottom of the cells. The image is postprocessed by subtracting a plane to correct for tilt and additionally correcting each scan line individually by a subtracted slope.

At each pixel, we perform a force spectroscopy measurement and a typical plot of the force F against time t, i.e., approach and retraction, is shown in Fig. 2(b) (right, black). We indent the sample by lowering the piezo height of the AFM [Fig. 2(b) (right, blue)] up to a predefined force, the so-called set point. This maximum force is chosen such that the deformation of the cortex is not impaired by the nucleus or substrate. Hence, we ensure not to indent the sample more than 20% of the full sample height [45]. For an average height of 10 μm for MDCK II cells, this percentage corresponds to a value of 1–2 μm [2]. In comparison to typical indentation depths used for investigating the actin cortex [45], we indent slightly more deeply to additionally also measure the keratin cortex and choose a set point of 2 nN. As previously shown for MDCK II cells, up to an indentation depth of 2.5 μm and a set point of 2 nN, the force indentation curves overlap, ensuring identical elasticity [46]. We chose a probe size and a step size of 2 μm to enable mechanical measurements of the cortex [45,47] while providing sufficient resolution for imaging. Of note, we manipulate the cells by applying a lateral strain with the cell stretcher (area change $\Delta A = A_{\text{new}} - A_0$), and then probe the viscoelastic properties of the cells by indenting with the AFM cantilever (area change $\Delta S = S_{\text{new}} - S_0$).

Figure 2(c) describes the timeline for a typical experiment. The total experiment time adds up to around 2 h per strain position including any overhead time during change in strains. Increasing the strain takes less than 2 min. In total, a typical experiment takes 6 h from starting the stretching experiment to finish when reaching the highest strain. Experiments are stopped prematurely, if the PDMS membrane breaks.

In addition to the force mapping, we take phase contrast microscopy images of the cells at each strain position and segment the cells [Fig. 2(d)]. By combining the AFM images and the light microscopy images, we can use the latter to segment the cells in the AFM images. To do so, we interpolate the segmented outlines to fit the AFM pixel size. We overlay the outlines on the AFM image and manually translate it to align the cell outlines with the respective cells on the AFM image. Afterwards, we determine the "inside" region of the cells [Fig. 2(e)], which includes only the cell center up to three pixels away from the cell outline (Fig. S4 in the Supplemental Material [39]). Altogether, we compare six conditions: two cell lines (WT and KO) and three strains (no strain, intermediate strain, high strain). Per condition, we collect 700 to 4000 force curves from 10 and 11 independent experiments for KO and WT cells, respectively.

We exclude those curves where the viscoelastic fit provides values that do not make sense from a theoretical point of view, such as values of the fluidity β smaller than 0, or an apparent compressibility modulus or prestress multiple orders

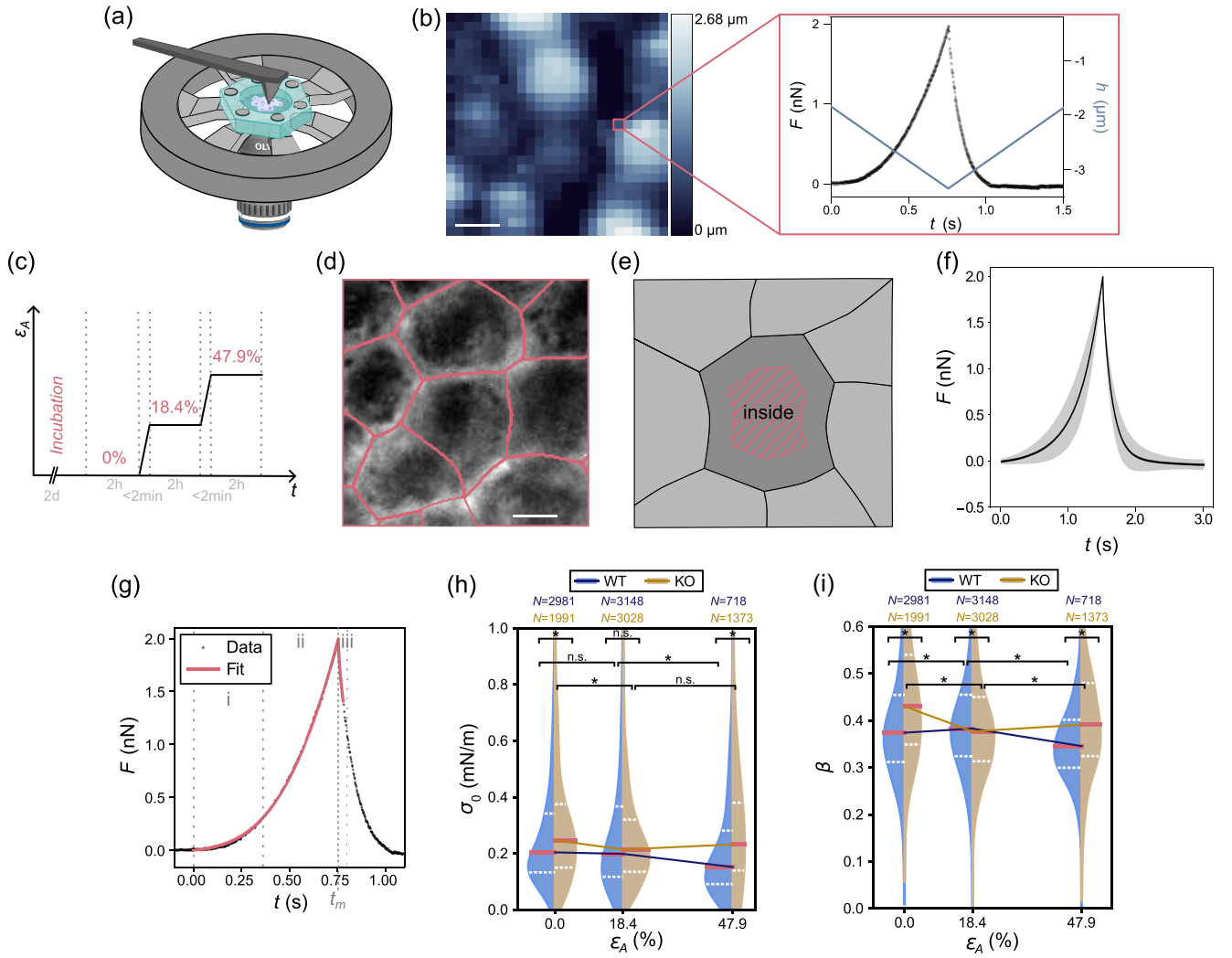

FIG. 2. AFM indentation experiments. (a) Schematic of the cell stretcher with the AFM cantilever (dark gray) approaching from above, and the light microscopy objective from below. The cells (purple) are grown on the stretchable PDMS membrane (cyan). (b) Left: Typical topography image of a confluent cell monolayer showing the sample height differences. Scale bar corresponds to 10 µm. Right: At each pixel, the cells are indented by changing the piezo height (blue) and a curve of the force F against time t is recorded (black). (c) Sketch of the timeline of a stretching experiment. The cells are seeded two days before the experiment. On the day of the experiment, each strain position is held for 2 h, allowing us to image and indent the cells to perform AFM force spectroscopy. Reaching the next strain position takes less than 2 min. (d) Example phase contrast image of the cells with the segmentation (pink). Scale bar corresponds to 10 µm. (e) Schematic of the inside region (pink hatched area) of the cell considered for the analysis. (f) Mean force curve (black, $N = 736$ individual data curves) and the standard deviation (gray shaded area) for the example of WT cells at 47.9% area strain. (g) An example plot of the force F against time t (black circles) together with a fit describing a viscoelastic model of the mechanical properties (pink line) and the different regions of the fit: Low indentation depth (i), high indentation depth (ii), and relaxation curve (iii). The time of maximum indentation is marked with t_m. (h) The prestress σ_0 and (i) the fluidity β of MDCK II cells at different strains ε_A. Data for WT cells are shown in blue; data for KO cells are in yellow. The lines on the violins represent the median (solid pink line) and the upper and lower quartiles (dashed lines). The medians are connected via solid lines and the number of force curves N is displayed in the figure in the respective colors. Statistical significance (* indicates $p < 0.05$; n.s. indicates "not significant") was tested by a Kruskal-Wallis test with a post hoc Dunn's test.

of magnitudes larger than the expected values that indicate a failed fitting of the curve. As expected for a complex biological system, we observe cell-to-cell variations as well as a distribution of the data curves even within one cell. Figure 2(f) displays a typical example of the mean force curve of all force curves within one condition (black) together with the standard deviation (shaded area). The force curves and their resulting average of all data categories are shown in Figs. S5 and S6 in the Supplemental Material [39].

To quantify the indentation data, we fit the force-time curves obtained from the AFM experiment using the viscoelastic Evans model, which is explained in detail in Refs. [48,49] for a spherical indenter. This model takes into account the geometrical shape of the sample. For a cell in a monolayer, this shape is approximated as a spherical cap in the center of the cell, here called the "inside" region.

In the Evans model, the sample is defined via a generic shape function $\tilde{g}_{\mathrm{cap}}$ of a deformed sphere as a function of

indentation depth. For a spherical indenter with radius R_p on a spherical cap with radius R_1, this function becomes

$$\tilde{g}_{\mathrm{cap}}(R_p, \varphi, \tilde{z}) = \frac{\sin\varphi + \tilde{R}_i \sin\left(\arctan\left(\frac{\tilde{R}_i}{\sqrt{\tilde{R}_p^2 - \tilde{R}_i^2}}\right)\right)}{1 - \tilde{R}_i^2} - \sin\varphi, \quad (3)$$

with $\tilde{R}_p = R_p/R_1$ the dimensionless radius of the probe, $\tilde{R}_i = R_i/R_1$ the dimensionless contact radius with the indenter, and φ the contact angle changing with indentation depth $\tilde{z} = z/R_1$. A sketch of the geometry can be found in Fig. S7 in the Supplemental Material [39].

The cortex is assumed to resist deformations only by the tension σ. σ includes the prestress σ_0, which the cortex naturally exhibits due to actomyosin contraction [6,50] and the membrane attached to the cortex [51,52], as well as the area compressibility modulus K_A as the response function to area dilation, assuming constant volume [52,53]:

$$\sigma = \sigma_0 + K_A\alpha, \quad (4)$$

with the area strain of the substrate $\alpha = \frac{S_{\mathrm{new}} - S_0}{S_0}$, where S_0 is the area before indentation and S_{new} is the area after indentation. The viscoelasticity is included through a power law for the compressibility modulus,

$$K_A = \widetilde{K}_A \left(\frac{t}{t_0}\right)^{-\beta}, \quad (5)$$

where $\widetilde{K}_A$ is the apparent area compressibility modulus and $t_0 = 1$ s (arbitrarily chosen).

The force response is then given by applying the elastic-viscoelastic-correspondence principle [29,48,54] as

$$f = 2\pi\tilde{g}_{\mathrm{cap}}(\tilde{z})R_1\left(\sigma_0 + \int_0^t \widetilde{K}_A\left(\frac{t-\tau}{t_0}\right)^{-\beta}\frac{\partial\alpha(\tau)}{\partial\tau}\mathrm{d}\tau\right). \quad (6)$$

The integrals can be approximated through a polynomial $[\alpha(\tilde{z}) = \sum_{n=1}^{m} d_n\tilde{z}^n]$ and divided into the force response to indentation, i.e., the approach curve $f_{\mathrm{app}}(t) = f(t \leqslant t_m)$ until the time of maximum indentation t_m [see Fig. 2(g)] and upon retraction $f_{\mathrm{ret}}(t) = f(t > t_m)$ starting at the time of maximum indentation t_m. The resulting equations are used to fit the experimental force-time curves in a piecewise manner [Fig. 2(g)] to obtain the prestress σ_0, the scaling parameter or apparent area compressibility modulus $\widetilde{K}_A$, and the power-law exponent or fluidity β. Thirty percent of the retraction part of the curve are included in the fit.

The prestress of the cortex is measured as the immediate response of the cell to the indentation at small times and indentation depths [Fig. 2(gi)], while the area compressibility modulus is measured when compressing the cell [Fig. 2(gii)]. Finally, the fluidity is mainly determined through the relaxation part of the force response of the cell [Fig. 2(giii)], although the parameters are not independent of each other Eqs. (4) and (5) [49].

Figures 2(h) and 2(i) show the results for the prestress and fluidity at increasing area strains ε_A as violin plots. We find the prestress to be higher in KO cells, compared to the WT cells [Fig. 2(h)]. This result first seems counterintuitive as one may expect the prestress to decrease when the keratin is removed in the KO cells as there is less material that is deformed when indenting. However, as we use stable KO cells, it is likely that the cells react to the loss of keratin, for example, by alterations to the actin cortex [55] and hence a change in the cortex contractility. Increased cortex contractility results in smaller cells as discussed in Ref. [52] and shown in Fig. 1(d), left, supporting this argument. Alternatively, but not contradictory, the cells might overcompensate the absence of the keratin with an increased amount of actin in the cortex, hence increasing the cortical tension. When comparing the prestress for the different strains applied to the cells, we find a decrease of σ_0 from the relaxed state (0% area strain) to the intermediate strain (18.4% area strain) for the KO cells, whereas this decrease occurs only for the high strain (47.9% area strain) in WT cells [Fig. 2(h)]. Of note, previous work indicates that the prestress depends only weakly on the cell size [29], and, likewise, the Young's modulus of confluent cells within the size range considered here shows no significant dependence on surface area [56]. We therefore expect no influence of the cell size variability observed in our experiments [Fig. 1(d)].

Likewise, the fluidity in WT cells changes little for intermediate strain and decreases at high strain, while in KO cells it strongly decreases already at intermediate strain and then remains at a similar value for the highest strain [Fig. 2(i)]. To rule out a remodeling of the cytoskeleton or relaxation of the PDMS on the timescale of the measurements, we analyze the data in a time-resolved manner and do not see any dependence; see Figs. S8(a) and S8(b) in the Supplemental Material [39]. Thus, the KO cells respond already to intermediate strains, whereas in WT cells the interplay between the actin and keratin networks preserve the original prestress and fluidity at these intermediate strains. The resilience of the actin network to the loss of keratin is remarkable, but at the same time, these results strongly indicate that KO cells mechanically respond to the loss of keratin.

Mechanical integrity, even under external influences is crucial for a cell to maintain its functions. For example, it has been shown that the cell can vary its surface area to keep the fluidity value constant [29]. Additionally, keratin has been revealed to be the main component for mechanical resilience in keratinocytes [11]. An increase in fluidity is often found in cancer cells or during wound healing [57,58]. For the cell, it is important to remain deformable enough to adapt to changes but if the fluidity is too high the cell might lose the ability to keep its shape and functions. The actin cortex is well able to respond to the loss of keratin and partially mimic the mechanical behavior of the WT cell. However, our findings indicate that, also in MDCK II cells, the keratin network plays an important role in ensuring cell integrity and preserving the overall mechanical properties of the cell and the keratin network stabilizes the cells by delaying the effect of stretching on the cells.

C. Three-dimensional tissues from WT cells form tighter cell layers than KO tissues

As the KO cells exhibit a smaller cell size and increased prestress, as well as a more sensitive response to strain, we hypothesize that the actin cortex in the KO cells is remodeled in response to the loss of keratin. To investigate this

hypothesis, we perform high-resolution imaging using STED microscopy of the actin cortices in 3D WT and KO tissues; see Figs. 3(b) and 3(c). MDCK II cells readily form 3D tissues when providing an extracellular matrix, such as hydrogels [59]. In particular, the cells grow into so-called cysts by forming a spherical shell that encloses a lumen in the center. In a cyst, the apical side of the cell faces the lumen [60] [see Fig. 3(a), cyan], in contrast to monolayers where the apical side forms the top of the cell layer. Because of the cyst's spherical geometry, a lateral cross section through its axial center reveals side views of the cells. In this orientation, the apical-basal axis lies within the imaging plane, enabling high-resolution imaging of the actin cortex along this axis with a standard STED microscope that improves lateral (but not axial) resolution. We first acquire a confocal microscopy image of the respective cross section of the entire cyst [see Figs. 3(bi) and 3(ci)] and then select the apical side of a single cell for high-resolution imaging [see Figs. 3(bii) and 3(biii) and Figs. 3(cii) and 3(ciii)]. We find that in the WT cells, the cortex is a thin, homogeneously distributed structure, whereas the KO cells exhibit a more irregular structure with bundles of actin pointing outwards the cell towards the lumen [Figs. 3(cii) and 3(ciii), pink arrows]. An additional example is shown in Fig. S9 in the Supplemental Material [39]. The intensity profiles shown next to the STED images confirm the qualitative assessment that the actin cortex in WT cysts is much smoother than in KO cysts. Hence, the KO cells indeed respond to the loss of the keratin with a change in their cortical structure. This change might result in an increase in the actomyosin contractility and consequently the prestress.

These interesting results lead to the question of what the immediate response of the cell layers at the beginning of the stretching process is. With the equibiaxial stretcher, this process is not accessible, as it is necessary to realign the field of view during the stretching process to image and measure the mechanical properties of the same cells at varying strains, which leads to a delay in the experimental process. Additionally, as we grow the cells into a confluent monolayer in the PDMS device, we only investigate a small section of the tissue. To overcome these limitations, we develop a complementary method to stretch whole MDCK II cells, grown into cysts, fast to high equibiaxial strains while imaging the entire tissue throughout the full process.

We increase the intraluminal pressure of living cysts using microinjection to enforce a stretching of the cell shell. Inspired by Wang, Zhao *et al*. [61], we inject insoluble mineral oil into the lumen of the cysts to stretch the cells [see Fig. 3(d)]. By stretching the cysts through oil injection, we apply the strain on the cells from the apical side. As it was shown before that the apical side of the cells is softer and dissipates the energy through the tissue to prevent damage, while the basal side of the cells provides elasticity to the system [62], the stretching from the apical side might result in a different response of the cells than monolayer stretching. Furthermore, we image the side view of the full tissue that is exposed to strain in comparison to the small field of view from the top when imaging the monolayer. Therefore, the combination of both stretching methods and imaging approaches offers complementary information.

We perform the injection on an inverted microscope which allows us to take phase contrast videos during the complete injection process. To stretch the cysts, within 1–3 s, we carefully inject mineral oil using a micropipette [see Fig. 3(d), gray]. Finally, the pipette is pulled out of the cyst. Figures 3(e) and 3(f) show phase contrast microscopy images of WT and KO cysts, respectively: unstrained, relaxed cyst (i), strained, injected cyst (ii); note that the example images after injection (ii) do not correspond to the same oil volume or area strain. Example videos of the injection of a WT and a KO cyst are provided as Movies 1 and 2 in the Supplemental Material [39]. We perform 10 independent experiments each, where one Petri dish with multiple cysts is considered one experiment. We inject oil into 27 WT and 28 KO cysts, respectively.

A visual inspection of the phase contrast images of both WT and KO cysts reveals that the KO cysts are smaller than the WT cysts; see Figs. 3(e) and 3(f). To rule out effects of the growth time on the size of the cysts we compare both cell lines at the same time span range after seeding. A manual estimation conducted by counting the nuclei in the imaged plane [Fig. 3(a)] confirms that the cysts in both cell lines contain approximately the same number of cells. To investigate the response of WT and KO cysts to stretching, we determine the cyst size at increasing oil volumes. The analysis workflow is schematically shown in Fig. S10 in the Supplemental Material [39] and described under Materials and Methods.

Figure 3(g) shows the cyst volume V_{cyst} with increasing oil volume V_{oil}. The WT cells are displayed in blue by a solid line and the KO cells in yellow by a dashed line. The lines display the mean over all cysts and the 95% confidence bands are presented as the shaded areas in the respective colors. In agreement with our visual impression, the quantitative analysis reveals that the KO cysts are indeed smaller than the WT cysts. This result supports our findings from above that the actin cortex in the KO cells exhibits a higher contractility: An increase in the tension increases the pressure on the lumen and consequently results in a smaller lumen, see Figs. 3(e) and 3(f). To quantitatively compare the change in cyst volume in WT and KO cysts with increasing oil volume, we define $\upsilon = \mathrm{d}V_{\mathrm{cyst}}/\mathrm{d}V_{\mathrm{oil}}$ as the slope of the respective mean curve for an oil volume from 0 nl to 0.01 nl; see Fig. 3(g) (pink lines). The KO cysts are stretched at $\upsilon = 1.20 \pm 0.04$ ($\pm$SE) while the WT cysts show $\upsilon = 1.94 \pm 0.05$. We thus find that both WT and KO cells respond in a similar manner to the increasing oil volume despite the different starting sizes. Figure S9(c) in the Supplemental Material [39] shows the same data plotted against increasing surface area strain $\varepsilon_{\mathrm{SA}}$ calculated from Eq. (A3) and reveals the same result.

Figure 3(h) shows the shell thickness d_{shell} plotted against increasing surface area strain $\varepsilon_{\mathrm{SA}}$. We cut the data at a surface area strain of 30%, as we have too few curves for higher strains for the WT cells which results in high noise when averaged. Interestingly, the thickness of the shell is the same in relaxed KO cysts and WT cysts; see Fig. 3(h). Hence, keratin KO cells are well able to form a spherical lumen with a normal shell. Both WT and KO cysts increase in size when injecting oil and the shell becomes thinner, indicating a stretching of the cells, assuming a constant cell volume. This size change translates to a surface area increase of the cyst of up to 30% for the WT cysts and even up to 70% for the KO cysts indeed

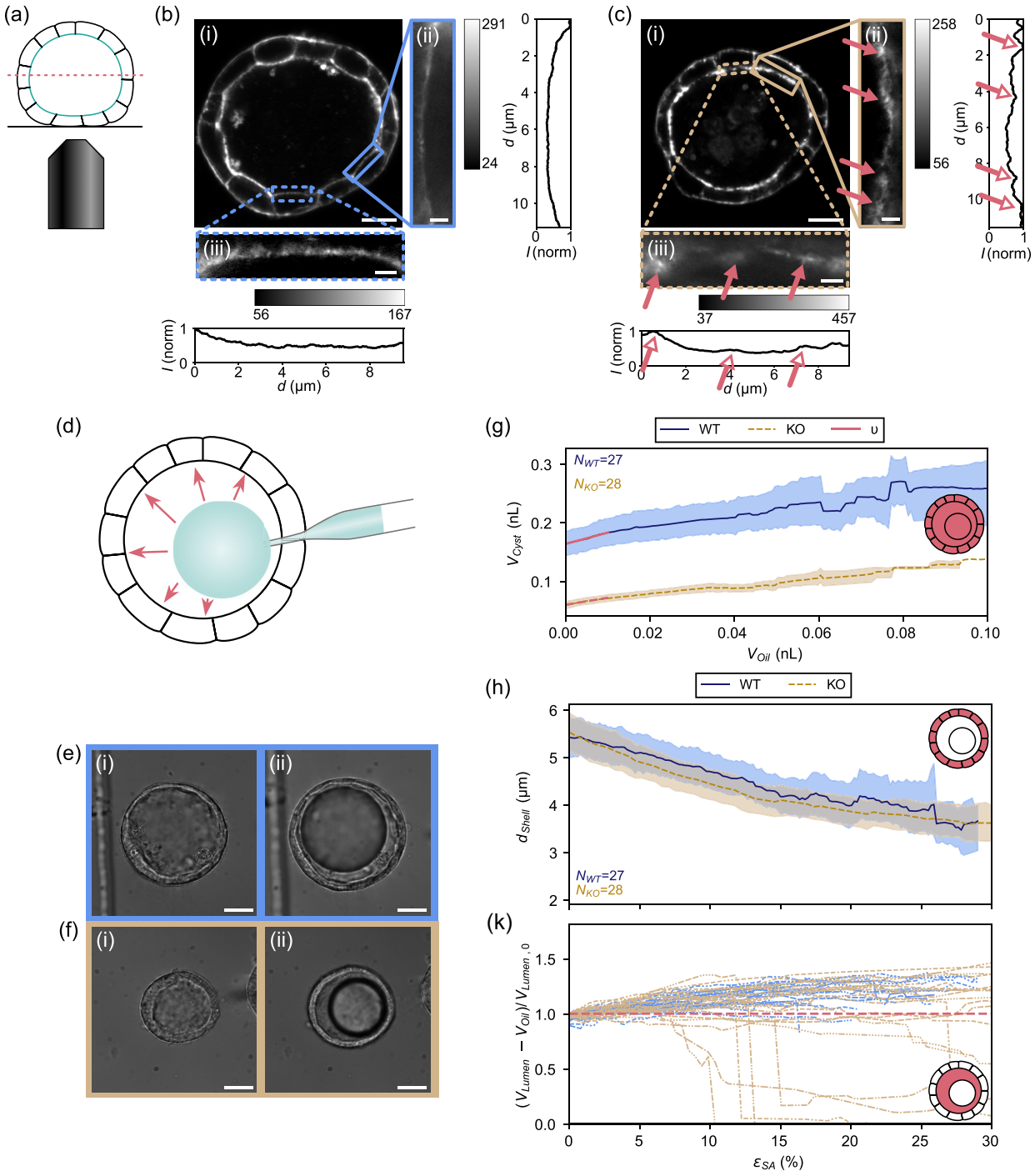

FIG. 3. Three-dimensional cysts grown from MDCK II cells. (a) Schematic side view of a cyst and the imaging plane (dashed pink line). The apical side of the cells (cyan) is facing the lumen. [(b) and (c)] Fluorescence images of the actin cortex in MDCK II cysts. (b) WT cyst. (c) KO cyst. (i) Confocal microscopy images of the lateral cross section of a cyst. Scale bars correspond to 10 μm. [(ii) and (iii)] STED microscopy images of the apical actin structure in a single cell including intensity profiles along the cortex. The pink arrows point towards irregular structures of the cortex in the KO cyst. Scale bars correspond to 1 μm. The gray scale bar shows the recorded signal in arbitrary units. (d) Schematic of the cyst injection. The micropipette (gray) is inserted into the cyst and the oil (cyan) is released into the lumen of the cyst (black) hence stretching the cyst (pink arrows). [(e) and (f)] Example phase contrast microscopy images of the WT and KO cells as cysts. (e) Living WT cyst. (f) Living KO cyst. (i) Unstrained cyst. (ii) Strained cyst. Scale bars correspond to 20 μm. (g) Cyst volume V_{cyst} (pink area in icon) plotted against increasing oil volume V_{oil}. The pink lines (solid, dashed) for small values V_{oil} denote the growth υ of the cysts. (h) Shell thickness d_{shell} (pink area in icon) plotted against increasing surface area strain $\varepsilon_{\mathrm{SA}}$. Lines are showing the mean of all datasets. The shaded area represents the 95% confidence interval. Results for WT cells are displayed in blue with a solid line, for KO cells in yellow with a dashed line. The number of cysts N is displayed in the figure in the respective color. (k) Normalized volume of the intraluminal fluid $V_{\mathrm{lumen}} - V_{\mathrm{oil}}/V_{\mathrm{lumen},0}$ plotted against increasing surface area strain $\varepsilon_{\mathrm{SA}}$ for each individual cyst. Data for WT cells are displayed in blue and for KO cells in yellow.

overcoming the limit of the cell stretcher with the maximum cell area increase in our experiments of 23%. Remarkably, both the shells of the WT and of the KO cysts thin in exactly the same fashion, starting from a shell thickness of around 5.5 μm [Fig. 3(h)].

To investigate tissue integrity, we next focus on the volume of the intraluminal fluid $(V_{\text{lumen}} - V_{\text{oil}})/V_{\text{lumen},0}$ and plot it against the surface area strain [Fig. 3(k)]. We normalize the volume of the intraluminal fluid by its value before injection, $V_{\text{lumen},0}$ for better comparability. Moreover, we show individual data curves rather than averages, because for the KO cysts (yellow), we observe two distinct populations: (i) cysts for which—similarly to the WT cysts (blue)—the volume of the intraluminal fluid remains constant throughout the stretching process; (ii) cysts, for which the volume of the intraluminal fluid suddenly drops to 0 at a strain between 10% and about 30%, i.e., the intraluminal fluid is pushed out of the cyst and replaced by the injected oil. These interesting differences between cysts grown from WT or from KO cells indicate that the WT cysts are leak-tight with well-developed cell-cell contacts and retain their intraluminal fluid. Therefore their volume increases by the injected oil volume. By contrast, a considerable fraction of the KO cysts become leaky upon stretching and readily release the intraluminal fluid as it gets replaced by the injected oil. We speculate that the missing keratin networks, which, in a rim-and-spokes geometry, connects the desmosomes, leads to impaired cell-cell contacts in the KO cysts. This is in agreement with intriguing investigations on free-standing, living cell monolayers that show rupture occurring for high strains at the cell-cell junctions and a weakening of the monolayer upon perturbation of the keratin IFs [36].

D. The keratin cortex ensures cell integrity at high strains

While these results demonstrate the overall importance of the keratin network for cellular integrity under strain, they do not address whether its protective effect varies within different cellular regions. As the MDCK II cells express keratin in a rim-and-spokes–like arrangement [9], the keratin network might add additional mechanical properties to the cell when comparing the periphery of the cells to the cell center. Hence, from the segmentation of the cells in our AFM data, we include an additional region and we divide each cell now into two regions: "rim" and "inside" [Fig. 4(a)]. From the segmentation, we obtain the outline of the cells right at the outermost pixels that are still included in that cell. The rim is defined as exactly this one-pixel-wide line. The inside region is defined as before, the cell center up to three pixels away from the rim. In between both regions, we exclude an interim area between the two regions to avoid any unclear classifications (Fig. S4 in the Supplemental Material [39]).

Figures 4(b) and 4(c) represent schematic side views (not to scale) of cells containing an actin (magenta) and a keratin (cyan) cortex (b) or only an actin cortex (c) and the indentation of the two different regions, i.e., the inside (left) and the rim (right) regions. An example 3D microscopy image of fixed WT cells shows this structure (Fig. S11 in the Supplemental Material [39]). In the inside region, we indent the cortex that is oriented perpendicularly to the indenting direction, forming a thin sheet. In the rim region, the keratin cortex connects to the desmosomes and is oriented in parallel to the indentation direction. As a result, the cantilever effectively indents more keratin and compresses the network in vertical direction and we expect a difference between the regions concerning the stiffness of the cells.

Although the cell shape is approximated as a spherical cap in the Evan's model, for a cell curvature that is large compared to the size of the cantilever, the cantilever encounters a close-to-flat surface. We apply this model also to the rim region of the cell. This is possible, because the diameter of the spherical indenter (2 μm) is small compared to the curvatures on top of the cell layer [see Fig. 4(d) for a line profile of the height of the cells and a cantilever (pink closed circle) schematically drawn to scale]. Note that the line profile shows height differences between the cell center and the cell-cell contacts rather than absolute height values.

Figure 4(e) shows the apparent area compressibility modulus at increasing area strains ε_A as violin plots. The compressibility modulus describes how much pressure is needed to achieve the compression of the cell and is hence a measure for the stiffness of the cell. As guide to the eye, the medians are connected with solid lines for the inside region and dashed lines for the rim region. Further violin plots comparing different pairs of datasets and the prestress as well as the fluidity are shown in Figs. S12–S14 and dataset S1 in the Supplemental Material [39].

We find the area compressibility modulus $\widetilde{K}_A$ to be increased in the rim region of both WT and KO cells compared to the inside region in the relaxed state [Fig. 4(e)]. In the rim of the cells, more force is needed to compress the cortex as here the cantilever not only deforms the cortical networks that form a thin sheet, perpendicular to the indentation direction, but also compresses the part of the cortex that lies in parallel to the indentation direction, i.e., the adherens belt [Figs. 4(b) and 4(c), right]. Hence, there is more effective cortex in the rim region both in the cells with and without keratin increasing the stiffness on the cell-cell contacts. Remarkably, the difference between rim and inside is much more pronounced for the WT cells, which can be attributed to the stiffening of IF under compression as shown for vimentin *in vitro* and in cells [26].

In the inside region, the cells are easier to deform, meaning that the cell is softer. This result supports our assumption above of less effective cortex compared to the rim region. Furthermore, the compressibility modulus of the KO cells increases steadily with the strain, while in the WT cells the modulus only increases from the relaxed state to the intermediate strain and is preserved from the intermediate strain to the high strain [Fig. 4(e)]. Cells stiffen during various processes, such as cell division or movement presumably through an activation of the myosin motors or cross-linking of the networks [63,64]. Both actin filaments and IFs are known to contribute to the stiffening [63]. At intermediate strains, the cell stiffens to stabilize the cell, whereas at high strains, this stiffening does not continue further likely to keep the cell's ability to deform and adjust to internal and external changes. It is remarkable that in the keratin KO cells the actin cortex remodels in response to the loss of keratin to fulfill the same purpose of stiffening, although the stiffness is decreased in the rim region. However, at high strains, when the actin filaments start to rupture [14,17] and the actin network fluidizes, the

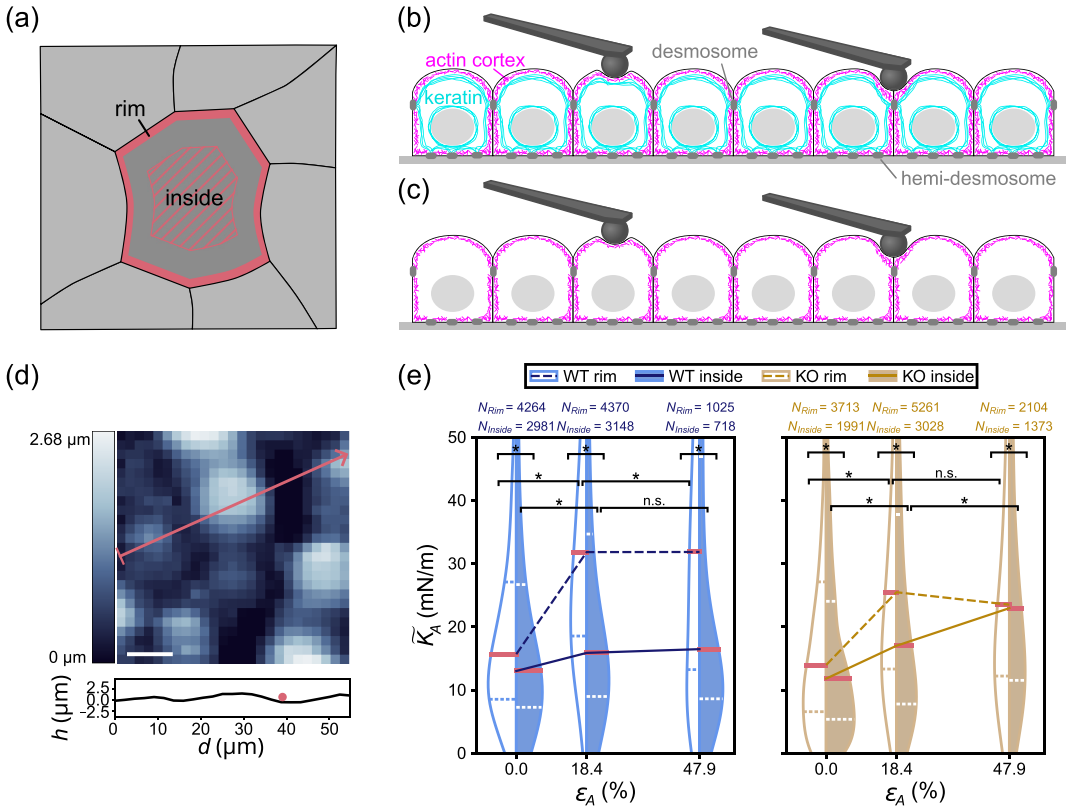

FIG. 4. Viscoelastic response of different cell regions. (a) Schematic of the division of the cell area into two regions: rim (thick pink line) and inside (pink hatched area). In between both regions, an interim section is excluded from the analysis. (b) WT. (c) KO cells; schematic side view (not to scale) of the actin cortex (magenta), keratin network (cyan), desmosomes and hemidesmosomes (dark-gray) and nucleus (gray) in WT cells that are indented with a cantilever (black) in the cell center (left) and at the cell-cell contacts ("rim" of the cell) (right). (d) An example line profile (pink line) of the height of the cells is shown together with the spherical indenter of radius 1 µm (pink circle) drawn to scale. Note that the line profiles shows height differences between the cell center and the cell-cell-contacts rather than absolute height values. Scale bar corresponds to 10 µm. (e) The apparent compressibility modulus $\widetilde{K}_A$ of MDCK II cells at different strains ε_A. Data for WT cells are shown in blue, data for KO cells in yellow. Filled violins correspond to the inside region of the cells, open violins with colored outlines to the rim region. The lines on the violins represent the median (solid pink line) and the upper and lower quartiles (dashed lines). The medians are connected via lines: Dashed lines for the rim region and solid lines for the inside region. The number of force curves N is displayed in the figure. Statistical significance (* indicates $p < 0.05$; n.s. indicates "not significant") was tested by a Kruskal-Wallis test with a post hoc Dunn's test.

interplay of the keratin network and the actin cortex is necessary to avoid a further stiffening to preserve the functions of the cell.

III. CONCLUSION

We present two complementary methods to investigate the effect of stretching on cells: an equibiaxial cell stretcher and microinjection of cysts. We study two lines of MDCK II cells, i.e., with (WT) and without (KO) keratin. We find that the keratin-deficient cells are well able to form tissues, both monolayers and cysts, and they follow and survive the high strains applied here, similarly to the WT cells. High-resolution imaging shows that the actin cortex structure in the KO cells is altered. Remarkably, the unstretched KO and WT cells are smaller but both exhibit the same thickness, as we see in the shell thickness of the cysts, hence the total volume of the KO cells is decreased.

The equibiaxial stretcher is compatible both with light and atomic force microscopy, enabling us to measure the mechanical properties of the sample while imaging the cells. We perform force mapping experiments, combining AFM imaging with spatially resolved force spectroscopy and overlay the AFM images with the light microscopy images to divide the cells into two regions according to the rim-and-spokes hypothesis. This approach enables us to compare the mechanical properties of the two regions. By fitting a dedicated model to the data, we determine the viscoelastic properties of WT and KO cells to investigate the influence of the keratin cortex on cell mechanics. Our results suggest that in KO cells the actin network is remodeled in response to the missing keratin network to maintain function, leading to an increase in prestress compared to the WT cells. This result is supported by the fact that the KO cells are smaller and form smaller cysts.

We compare an "intermediate" and a "high" area strain. For both the prestress and the fluidity we observe that the KO cells display altered mechanical properties already at the intermediate strain, whereas for WT cells, the actin and keratin networks in concerted action are able to maintain the original,

i.e., unstrained, values and react only to the high strain. The KO cysts react more sensitively to the stretching process than the WT cysts, and become leaky upon stretching. This is a particularly important finding since the increase of Laplace pressure due to oil injection results in a critical loading of cell-cell contacts responsible for barrier function of the epithelial tissue. Lack of keratin leads to early rupture of the cell-cell contacts, while its presence keeps the barrier properties of the tissue intact with pivotal implications for the biological function of the renal tube. Taken together, our results show the necessity of the keratin network to stabilize cell layers under strain.

ACKNOWLEDGMENTS

We thank Ruben Haag, Peter Luley, Angela Rübeling, Mihaela Raycheva, Greta Höhndorf, Marie Tersteegen, Lara Köpping, Axel Munk, Timo Betz, and Jonathan Frohn for technical support and fruitful discussions. This work was funded by the Deutsche Forschungsgemeinschaft (DFG, German Research Foundation): Project-ID 449750155-RTG 2756, Projects A2 and A7 (to S.K.), Projects A6 and B1 (to A.J.); Project-ID 430255655-KO3572-8/1 (to S.K.); Project-ID 449544493 (to S.K.); Project-ID 390729940-EXC 2067/1 (to S.K. and A.J.). The work was further financially supported by the European Research Council (ERC, Grant No. CoG 724932, to S.K.) and this research was conducted within the Max Planck School Matter to Life, supported by the German Federal Ministry of Research, Technology and Space (BMFTR, Grant No. M526300) in collaboration with the Max Planck Society.

S.K. conceived and supervised the project; R.M. performed the AFM experiments; R.M. and U.U. performed cyst stretching experiments; R.M. and P.J. performed STED imaging; S.K., A.J. and C.G. supervised the work; R.M. analyzed the data; U.R. prepared the fluorescently tagged cell lines, and performed the cell culture, the immunostaining and fluorescence microscopy; N.S. prepared the KO cell line; A.P.-T. provided analysis code; A.V.S. characterized the cell-stretcher; A.J. developed the viscoelastic model; R.M., S.K. and A.J. interpreted the results; R.M. and S.K. wrote a first draft of the manuscript, all authors contributed to writing the manuscript.

DATA AVAILABILITY

The data that support the findings of this article are openly available [65].

APPENDIX: MATERIALS AND METHODS

1. Cell stretcher

The home-built stretcher [see Fig. 1(a)] consists of a motorized internal gear ring (dark gray), controlled by the software "spec" (Certified Scientific Software, Cambridge, MA, USA), to which six arms (light gray) are connected via gears. With each motor movement, the gear ring is turned (large pink arrow) resulting in an outwards movement of the arms (small pink arrows) that hold the PDMS device, thereby stretching the device equibiaxially. To ensure unhindered movement and preventing tearing of the device while the arms are turning, the holes in the device are stabilized by poly(tetrafluoroethylene) (PTFE) sleeves: see Fig. S1(b) in the Supplemental Material [39]. During cell culture and in preparation of the stretching experiments, the PDMS device is kept in a prestretcher consisting of a PTFE ring with six pins fitting into the PTFE sleeves in the device and a transfer aid. Thus, the membrane within the PDMS device is kept even and all membranes are set to the same fixed strain at the beginning of the experiments. The transfer aid made from stainless steel is situated between the prestretcher and the device and provides a seamless transfer from the Petri dish to the stretcher by ensuring a smooth sliding off of the pins of the prestretcher onto the arms of the stretcher.

2. PDMS devices

We fabricate PDMS (Sylgard 184, Dow Chemical, Midland, US) devices with a total diameter of 3.25 cm; see Fig. S1(a) in the Supplemental Material [39]. They consist of a membrane with a thickness of 250 μm. The walls have a height of 0.5 cm and delimit a well of radius 0.5 cm on the membrane into which the cells are seeded. Previous studies reported that PDMS Sylgard 184 has a storage modulus that well exceeds the loss modulus and therefore essentially behaves as an elastic solid showing Hookean behavior [30,31,66,67].

To fabricate the walls of the devices, 3 g of PDMS base are mixed with cross-linker at a ratio of 25:1, filled into home-made hexagonal molds made from polylactic acid (Polymaker, Shanghai, China), cured for 1.5 h at 65 °C and removed from the mold. We produce the membranes in two layers. PDMS is mixed with cross-linker at a ratio of 25:1, spin-coated onto a 4-inch Si-wafer (ramp up to 60 rpm within 10 s, 10 s at 60 rpm) to obtain a thickness of 220 μm and cured for 45 min at 65 °C. The membrane is plasma activated (Zepto, Diener electronic GmbH & Co. KG, Ebhausen, Germany) at 30 W for 21 s. Dark-red fluorescent microspheres (660/680 nm, 2% solids, FluoSpheres F8807, 200 nm, Invitrogen, Waltham, MA) are diluted in a ratio of 1:200 in isopropanol and spin coated onto the membrane (ramp up to 60 rpm within 25 s and 25 s at 60 rpm). A second layer of PDMS with a mixing ratio of 25:1 is spin coated onto the same wafer (ramp up to 2460 rpm within 40 s and 20 s at 2460 rpm) to obtain a thickness of 30 μm.

We place the cured PDMS walls onto the uncured PDMS membrane, cure everything together for 45 min at 65 °C and remove the device from the wafer. Holes are punched into the wall using a 4-mm biopsy puncher (Roth, Karlsruhe, Germany) and the PTFE-sleeves are inserted. The finished PDMS devices are boiled in water for 1 h and stored in sterile water for at least 8 h. This step ensures that the PDMS device is sterile for cell culture and that the device is soaked with water to prevent the cell medium from being absorbed by the device.

In preparation for the cell experiments, the prestretcher is assembled and added to the PDMS device (Fig. S1(b) in the Supplemental Material [39]). The well inside the device is rinsed with phosphate-buffered saline (PBS), coated with laminin (25 μg/ml, from mouse; Gibco, Life Technologies, Carlsbad, CA) for 1 h at room temperature and rinsed again with PBS.

3. Cell culture

All experiments are performed on Madin-Darby Canine Kidney cells strain II (MDCK II, ECACC 00062107, European Collection of Authenticated Cell Cultures, Salisbury, UK). We stably transfect the cells with a bicistronic vector to allow for coexpression of K8-EGFP and lifeact-mCherry (VectorBuilder, Neu-Isenburg, Germany); this way, we fluorescently tag both the keratin and the actin structures. We work with a polyclonal cell line. About 30% of the cells are actually transfected. For fluorescence microcopy experiments, we specifically chose transfected cells. For the AFM experiments, all cells are measured. In the following, we will refer to these cells as WT cells. The keratin 8 KO cells are produced using CRISPR/Cas9n technology. We clone two different gRNAs targeting exon 1 of the canine Krt8 gene into PX462 V2.0 vector (Addgene No. 62987, Watertown, MA; kind gift of Feng Zhang) [68]. The sequences of the gRNAs are gRNA-1: 5′-GGG GCT CAC CTT GTC GAT GAA GG -3′ and gRNA-2: 5′- GGG CGG GCA GTG CCT GGG GCT GG -3′. We cotransfect MDCK II cells with both vectors and subject isolated single cell clones to immunofluorescence analysis using anti-keratin 8 (TROMA-1, DSHB, Iowa City, IA, US) and anti-desmoplakin (DP-1, Progen, Heidelberg, Germany) antibodies and immunoblot analysis to confirm knockout (Figs. S2(c) and S2(d) in the Supplemental Material [39]). To test for a possible upregulation of IFs in the keratin K8 KO cells, we perform a staining against keratin and vimentin; see Fig. S2(e) in the Supplemental Material [39].

The cells are cultured in Eagle's minimum essential medium, supplemented with Earle's salts and 2 mM GlutaMax (Gibco) and 10% fetal bovine serum (Gibco) and kept at 37 °C and 5% CO_2. For the WT cells, we add 2 μg/ml Puromycin (Sigma Aldrich, St. Louis, MO, USA) to the medium. Twice per week, the cells are passaged, and passages 4 to 12 after thawing are used for the experiments.

Two days before the AFM experiments, we seed the cells on the PDMS devices to reach confluence for the experiments. To improve the image quality for fluorescence microscopy, the cell medium is replaced by phenol-free medium (Gibco) containing the same supplements as the regular culturing medium. Additionally, to be able to perform experiments without CO_2 supply, we add 15 mM HEPES (Thermo Fisher Scientific, Waltham, MA) to the cell medium.

To cultivate the cysts, we coat gridded Petri dishes (μ-dish, 35mm, low, Ibidi, Gräfelfing, Germany) by incubating them with laminin (20 μg/cm^2) for 1 h at 37 °C and 5% CO_2. For the following steps, all material including the cells are cooled to 4 °C. Fifty thousand cells, prepared in 450 μl medium and 50 μl Matrigel (Corning Inc., Corning, NY) are gently mixed. The solution is then transferred into the dish and incubated at 37 °C and 5% CO_2 for 7–9 days to allow for cyst formation.

4. Immunoblot analysis

Expression of keratin 8 in original, i.e., nontransfected, wild-type and in keratin 8 KO MDCK II cells is analyzed by immunoblotting. Polypeptides are separated by standard SDS polyacrylamide gel electrophoresis and transferred onto polyvinylidene fluoride Immobilon-P membranes (Millipore, Merck, Darmstadt, Germany) by tank blotting. The membranes are blocked with 1x RotiBlock (Roth) and incubated overnight at 4 °C with rat anti-keratin 8 (TROMA-1, DSHB) and rabbit anti-actin (Sigma Aldrich, A2066) antibodies. Membranes are washed in TBS-T buffer (50 mM Tris, 150 mM NaCl, 0.05% Tween 20, pH 7.6) and subsequently incubated with secondary antibodies (anti-rat HRP, anti-rabbit HRP, both from Dianova, Hamburg, Germany) for 1 h at room temperature. Bound antibodies are detected with SuperSignal West Pico PLUS Chemiluminescent Substrate (Thermo Fisher Scientific) and a chemiluminescence system (Fusion SL, Vilber Lourmat). On the same membranes keratin 8 and actin are detected consecutively. Bound antibodies are stripped by incubation of the membranes with stripping buffer (100 mM glycine, pH 2) three times for 20 min.

5. Cell fixation, immunofluorescence staining and fluorescence imaging

For the imaging of the actin and keratin 8/18 networks in both cell lines, the cells are seeded in advance on cover slips (diameter of 18 mm, thickness 1.5H, VWR, Radnor, PA, US). When the cells reach confluence, they are washed with PBS and fixed with 4% formaldehyde (Thermo Fisher Scientific) for 20 min at room temperature. Afterwards, the cells are permeabilized by washing briefly with 0.1% Triton X solution (Triton X-100, Sigma Aldrich, diluted with PBS). To stain the actin, phalloidin (Alexa Fluor 647, Invitrogen) is mixed with 0.1% Triton X solution in a ratio of 1 to 40 and added to the cells for 1 h at room temperature. Then, the cells are washed, first with 0.1% Triton X solution, and second with ultrapure water. Finally, the glass slides are mounted on a microscopy slide with mounting medium (ProLong Diamond antifade, Invitrogen) and stored at 4 °C for at least one day.

For imaging the keratin and vimentin networks in both cell lines, the cells are seeded on cover slips (diameter of 18 mm, thickness 1.5H, VWR, Radnor, PA, US). When the cells reach confluence, they are washed with PBS and fixed with 4% formaldehyde (Thermo Fisher Scientific) for 10 min at room temperature. Afterwards, the cells are permeabilized by washing for 5 min with 0.2% Triton X solution (Triton X-100, Sigma Aldrich, diluted with PBS). Afterwards, the cells are blocked using 5% BSA blocking solution in PBS (bovine serum albumin 10%; Miltenyi Biotec, Bergisch Gladbach, Germany) for 30 min at room temperature. An antibody against cytokeratins K1, K2, K3, K4, K5, K6, K7, K8, K10, K14, K15, K16, and K19 (pan-cytokeratin monoclonal antibody conjugated with Alexa Fluor 488, Thermo Fisher Scientific) and an antibody against vimentin (anti-vimentin Alexa Fluor 647, abcam, Cambridge, UK) both diluted at a ratio of 1:100 with 2% BSA blocking solution in PBS are added and incubated for 1.5 h at room temperature. The cells are washed 3 × for 15 min with PBS at room temperature and briefly with ultrapure water. Finally, the cover slips are mounted on microscopy slides with mounting medium (ProLong Diamond antifade, Invitrogen) and stored at 4 °C for at least one day.

The fixed and stained cells are imaged on an inverse confocal microscope (IX83 with a Fluoview FV3000, Olympus, Hamburg, Germany) at 100× magnification (NA 1.45, UPLanXApo, Olympus) and laser line 640 nm for actin and

laser line 488 nm for keratin. z-Stacks are recorded with $\Delta z = 0.41$ μm.

For the high-resolution imaging of the actin networks in both cell lines, cysts are seeded in advance in Matrigel in Petri dishes (μ-dish, 35 mm, high, Ibidi) to reach confluence and allow for cyst formation. To remove the Matrigel from the cysts, Cell Recovery Solution (Corning Inc.) is added and incubated at 4 °C for 25 min. Cysts are washed with PBS and 1 μm staining solution (actin LIVE RED, abberior, Göttingen, Germany) is added to the sample and incubated for 60 min at 37 °C and 5% CO_2. Afterwards, the cysts are washed with PBS and 4% formaldehyde (Thermo Fisher Scientific, Waltham, MA, US) is added and incubated for 20 min at room temperature to fix the cells. Finally, the Petri dish is filled with PBS and stored at 4 °C until imaging.

STED imaging of actin networks in cysts is performed using a STEDYcon system (Abberior Instruments, Göttingen, Germany) mounted on an inverse fluorescence microscope (IX83, Olympus, Hamburg, Germany) with a 60× water immersion objective (NA 1.20, UPLanSApo, Olympus). The objective's correction collar is adjusted to account for the coverslip thickness of the Petri dishes used, thereby minimizing spherical aberrations. A 640-nm laser and a 775-nm laser are used for excitation and depletion, respectively, to acquire STED images with increased resolution in the lateral dimension compared to confocal images.

Epifluorescence imaging of the fluorescent beads for the characterization of the PDMS stretching devices is performed on a motorized upright fluorescence microscope (BX63, Olympus) at 60× magnification using a water dipping objective (NA 1, LUMPLFLN60XW, Olympus) with an Orca Flash 4.0 camera (Hamamatsu, Tokio, Japan) and a Sola SE II fluorescence lamp (Lumencor, USA) set to 15% power. We image the fluorescence microspheres using a Cy5 filter set (U-F49006, excitation: ET620/60x, dichroic mirror: T660LPXR, emission: ET700/75m; Olympus) at 50-ms exposure time. At each position, z-stacks are recorded with $\Delta z = 0.54$ μm.

6. Characterization of the cell stretcher and PDMS device

Characterization of the stretcher and PDMS stretching devices is performed without cells. The devices are filled with water. The device is stretched in motor steps of $\Delta \mathrm{mp} = 0.1$ a.u. until rupture. The strain rates are 0.46 s^{-1} for reaching the intermediate strain and 0.74 s^{-1} for reaching the high strain.

In the stretcher, the membrane tends to be uneven or tilted because it is manually placed on the stretcher arms (Fig. S15(a) in the Supplemental Material [39]). To overcome this problem, we record 3D epifluorescence images of the beads and correct the images for the tilt. As the beads are in one layer in the PDMS membrane only and the bead size is smaller than the difference in z between two images, for each lateral position there is only one z position where the beads are in focus. We compute a spatial Laplacian for every image for a kernel size of 5 pixels to define the sharpness. We normalize the Laplacian along the z axis with respect to the maximum absolute value in a pixelwise manner. Next, we determine which slice in the stack is in focus for a coarse grid of the image. The sum of the normalized, absolute gradient values is computed for each z-slice and grid block. A 2D matrix is then created storing the indices of the z-slice with the highest sum, representing the "best-in-focus" slices at each grid block (Fig. S15(b) in the Supplemental Material [39]). Finally, we fit a second-order 2D polynomial to the grid and interpolate the original z-stack to the result of this fit to create a tilt-corrected image. We repeat this procedure for every stack at every stretching position in the experiment to generate a time series (Fig. S15(c) in the Supplemental Material [39]).

For the calculation of the strain, we manually align the tilt-corrected images at all strains in the center (Fig. S15(d) in the Supplemental Material [39]). Using the python implementation "itk-elastix" of the software "Elastix" [69,70], every image in the image series of the beads is registered with respect to its previous image using an affine transformation (Fig. S15(e) in the Supplemental Material [39]).

This procedure is repeated for 20 independent experiments. The arithmetic mean and standard deviation of all datasets is calculated and the values for the linear strain in x direction from the averaging for each mp is used to determine the area strain [Eq. (2)], since $\varepsilon_x = \varepsilon_y$ applies for equibiaxial strain.

7. Atomic force microscopy

The force spectroscopy measurements are performed on a Nanowizard 4 AFM (Bruker Nano GmbH, MA, USA) combined with a manual or motorized inverse fluorescence microscope (IX73 or IX83, Olympus/Evident, Hamburg, Germany). Three different strain positions (0%, 18.4%, and 47.8% area strain) are included for the measurements and at each strain approximately the same region within the device is chosen. We use a cantilever with a spherical tip of 2 μm diameter (CP-PNPL-SiO-A, Nano and More GmbH, Wetzlar, Germany). The maximum force, i.e., the setpoint, is set to 2 nN and we use an indentation velocity of 2 μm/s. Force maps of size 50 μm × 50 μm with a pixel size of 2 × 2 μm^2 are recorded. At each strain position, we take four force maps to cover a total area of 100 μm × 100 μm. The measurements are performed in liquid in a heated environment at 37 °C (The Cube, Life Imaging Services, Basel, Switzerland). Humidification is provided by placing wet tissue paper close to the sample. Additionally, we add fresh medium with HEPES every 2 h to ensure a close-to-physiological environment for the cells and maintain the pH. Phase contrast images are taken at 20× magnification (NA 0.45, LUCPlanFLN, Olympus) with a monochromatic camera (UI-3060CP-M-GL Rev. 2, IDS Imaging Development Systems GmbH, Obersulm, Germany) and 50 ms exposure time. The experiments are terminated either after reaching the highest strain or when the PDMS device breaks.

8. Cyst injection

For the injection experiments, the outer edge of the Matrigel in the Petri dish is removed using a pipette and subsequently, the cysts are washed with PBS at 4 °C. Cell Recovery Solution (Corning Inc.) is added to the cysts and incubated at 4 °C for 25 min. Finally, the sample is washed with PBS and warm cell medium with HEPES (15 mM, Thermo Fisher Scientific) and penicillin/streptomycin [10 000 units/(10 mg/ml), Merck, Darmstadt, Germany] is added.

The experiments are performed on a motorized inverted microscope (IX81, Olympus) at 40× magnification (NA 0.95, UPLSAPO40X2, Olympus) and an XM10 camera (Olympus). To carry out the injection of the cysts, a microinjector (InjectMan NI2, Eppendorf, Hamburg, Germany) is used in combination with a micropipette with an inner diameter of 0.5 μm and an outer diameter of 1 μm (Femtotip, Eppendorf) and mineral oil for molecular biology ($\rho = 0.84$ g/ml, BioReagent, Sigma Aldrich). Before the injection, a phase contrast image of the cyst is taken. The tip is inserted into the cyst and oil is released into the lumen of the cyst at an injection pressure varying between 1000–6000 hPa for 0.5–6 s. The amount of oil injected into the cyst is determined by visually inspecting the cyst while injecting in order to reach a sufficient degree of strain, but avoid a rupture of the cyst. Once the oil droplet is big enough, the tip is pulled out of the cyst. During the whole injection process, we record a phase contrast video. In the end, a phase contrast image is recorded as before the injection. Within one Petri dish, up to four cysts are injected. In total, the time between removing the Matrigel and finally fixing the sample is at maximum 1 h. We repeat this procedure on 27 WT cysts and 28 KO cysts from 10 independent experiments each. When injecting WT cysts, in almost all cases nontransfected cells were chosen that comprise about 70% of the polyclonal mixture.

9. Image analysis

To analyze the area of the cells, cell segmentation is performed on the phase contrast microscopy images (field of view 300 × 300 μm^2) using the software "CellPose" [71] and its python implementation (Figs. S3(a) and S3(b) in the Supplemental Material [39]). We use the model "cyto2" [72] and the default flow threshold of 0.4 for all datasets; here one datasets corresponds to the data collected from one experiment. 11 datasets are used for the WT cells and 10 for the KO cells. The cell area is determined by summing over the number of pixels per cell and scaling with the pixel size of the images (Fig. S3(c) in the Supplemental Material [39]).

For the determination of the eccentricity and orientation of the cells, ellipses are fitted to the outline determined from CellPose using the python function "fitEllipse" in the package "cv2" (Fig. S3(d) in the Supplemental Material [39]). The eccentricity of the ellipse is calculated via its semimajor axis a and its semiminor axis b by

$$e = \sqrt{1 - \frac{b^2}{a^2}}. \tag{A1}$$

An eccentricity of 0 and 1 represent a circle and a parabola, respectively. Any value between 0 and 1 represents an ellipse. The orientation is defined as the angle between the semimajor axis a and the x axis from 0° to 180° as the direction is irrelevant (Fig. S3(e) in the Supplemental Material [39]).

To analyze the cyst shape in the cyst injection experiments over time, we use the video taken during the injection. The workflow is schematically shown in Fig. S10 in the Supplemental Material [39]. We manually segment the cyst, the lumen and the oil droplet in each individual image frame of the video (Fig. S10(a) in the Supplemental Material [39]) using the polygon tool in Fiji [73] to outline each part and convert the outline into a mask (Fig. S10(b) in the Supplemental Material [39]). We calculate the center of mass of the lumen (Fig. S10(c) in the Supplemental Material [39]), determine vectors $\mathbf{r}$ from the center of mass to the outline of the mask for 200 varying angles ϑ from $-\pi < \vartheta < +\pi$ and calculate the length of each vector (Fig. S10(d) in the Supplemental Material [39]). Subsequently, the mean of all vector lengths is calculated as the radius of the lumen r_{lumen}. We repeat the process to determine the radius of the cysts r_{cyst} with the same center of mass as the lumen. As the oil droplet is not necessarily positioned in the exact center of the lumen, the center of mass is calculated for the oil droplet separately (Fig. S10(c) in the Supplemental Material [39]) and the radius r_{oil} is determined in the same manner as for the lumen and cyst.

This procedure is repeated for every frame in the video, starting from one frame before the first oil droplet is released into the cyst until the stretching is finished, but before the micropipette is pulled out of the cyst (Fig. S8(e) in the Supplemental Material [39]).

Finally, the volumes of cyst, lumen, and oil droplet are determined with the assumption of a perfect sphere for each and the average thickness d of the shell is calculated by

$$d_{\text{shell}} = r_{\text{cyst}} - r_{\text{lumen}}. \tag{A2}$$

The surface area strain ε_{SA} of the cysts is calculated as

$$\varepsilon_{\text{SA}} = \frac{A - A_0}{A_0} = \left(\frac{r}{r_0}\right)^2 - 1 \tag{A3}$$

with the surface area of a sphere before (A_0) and during injection (A) and the radius of the cyst before (r_0) and during injection (r).

The intensity profiles of the actin cortices in WT and KO cysts were determined as the average of intensity values over the short side of the rectangle using Fiji [73], normalized by the maximum of the intensity, and plotted using python.

10. AFM data analysis

For the analysis of the force spectroscopy measurements, we preprocess the data curves using the python package "nanite" [74] (Fig. S16 in the Supplemental Material [39]). At first, a baseline correction is applied to the raw force curves (Fig. S16(a) in the Supplemental Material [39]), correcting its tilt and offset to the x axis (b). Next, the contact point is estimated using the nanite function "deviation from baseline" (Fig. S16(c) in the Supplemental Material [39]). Finally, the curve is corrected by the tip-sample separation, which separates the distance of the cantilever towards the sample from the deflection of the cantilever in the opposite direction (Fig. S16(d) in the Supplemental Material [39]).

The workflow for the analysis is shown schematically in Fig. S4 in the Supplemental Material [39]. We combine the data from the force spectroscopy measurements with the images from light microscopy. The phase contrast images are segmented with CellPose as described before (Figs. S4(a) and S4(b) in the Supplemental Material [39]). As the phase contrast images have a different pixel size than the AFM images, the resulting cell outlines are interpolated to fit the AFM pixel size (Fig. S4(c) in the Supplemental Material [39]). These outlines are then overlaid onto the AFM images where each pixel

contains a force spectroscopy curve (Figs. S4(d) and S4(e) in the Supplemental Material [39]). Each cell is divided into two regions using the outline. The outline traces the outermost pixels that are still part of the cell. The rim is defined as a single-pixel-wide line that marks this edge of the cell. The inside region is then identified as the area in the cell center extending three pixels inward from the rim (Fig. S4(f) in the Supplemental Material [39]). With this division, we exclude an interim region between the rim and the inside to avoid any unclear classification into either of these regions.

Finally, the curves are rated using the respective method implemented in nanite. We train our own neural network using the respective feature in nanite on force curves that are not included here in the further analysis to fit with our data and results. We exclude every curve with a rating lower than 4.5 to omit out any curves of low quality (Fig. S4(g) in the Supplemental Material [39]). Figure S4(h) in the Supplemental Material [39] shows a phase contrast image next to an overlay of the same image and the segmented cell outlines.

The force curves are averaged per category by aligning all curves on their maximum. Since the time points of the curves can be different, we interpolate the curves to correct the time axis. Finally, the mean and the standard deviation of the curves are calculated.

The individual curves are fitted with a viscoelastic fit providing the viscoelastic properties prestress of the cortex, apparent compressibility modulus and fluidity. After fitting each curve, we exclude those curves where the viscoelastic fit provides unphysical values and show a failed fitting of the curve.

We performed a Kruskal-Wallis test with a post hoc Dunn's test on the data.

[1] A. F. Pegoraro, P. Janmey, and D. A. Weitz, Mechanical properties of the cytoskeleton and cells, Cold Spring Harb. Perspect. Biol. **9**, a022038 (2017).

[2] A. R. Harris, L. Peter, J. Bellis, B. Baum, A. J. Kabla, and G. T. Charras, Characterizing the mechanics of cultured cell monolayers, Proc. Natl. Acad. Sci. USA **109**, 16449 (2012).

[3] D. A. Fletcher and R. D. Mullins, Cell mechanics and the cytoskeleton, Nature (London) **463**, 485 (2010).

[4] J. P. Conboy, I. Istúriz Petitjean, A. Van Der Net, and G. H. Koenderink, How cytoskeletal crosstalk makes cells move: Bridging cell-free and cell studies, Biophys. Rev. **5**, 021307 (2024).

[5] N. Wang, Mechanical interactions among cytoskeletal filaments, Hypertension **32**, 162 (1998).

[6] P. Chugh and E. K. Paluch, The actin cortex at a glance, J. Cell Sci. **131**, jcs186254 (2018).

[7] U. Rölleke, P. Kumari, R. Meyer, and S. Köster, The unique biomechanics of intermediate filaments—From single filaments to cells and tissues, Curr. Opin. Cell Biol. **85**, 102263 (2023).

[8] I. Szeverenyi, A. J. Cassidy, C. W. Chung, B. T. Lee, J. E. Common, S. C. Ogg, H. Chen, S. Y. Sim, W. L. Goh, K. W. Ng, J. A. Simpson, L. L. Chee, G. H. Eng, B. Li, D. P. Lunny, D. Chuon, A. Venkatesh, K. H. Khoo, W. I. McLean, Y. P. Lim, *et al.*, The human intermediate filament database: Comprehensive information on a gene family involved in many human diseases, Hum. Mutat. **29**, 351 (2008).

[9] R. A. Quinlan, N. Schwarz, R. Windoffer, C. Richardson, T. Hawkins, J. A. Broussard, K. J. Green, and R. E. Leube, A rim-and-spoke hypothesis to explain the biomechanical roles for cytoplasmic intermediate filament networks, J. Cell Sci. **130**, 3437 (2017).

[10] N. Schwarz, R. Windoffer, T. M. Magin, and R. E. Leube, Dissection of keratin network formation, turnover and reorganization in living murine embryos, Sci. Rep. **5**, 9007 (2015).

[11] L. Ramms, G. Fabris, R. Windoffer, N. Schwarz, R. Springer, C. Zhou, J. Lazar, S. Stiefel, N. Hersch, U. Schnakenberg, T. M. Magin, R. E. Leube, R. Merkel, and B. Hoffmann, Keratins as the main component for the mechanical integrity of keratinocytes, Proc. Natl. Acad. Sci. USA **110**, 18513 (2013).

[12] K. M. Stroka and H. Aranda-Espinoza, Effects of morphology vs. cell–cell interactions on endothelial cell stiffness, Cell. Mol. Bioeng. **4**, 9 (2011).

[13] E. A-Hassan, W. F. Heinz, M. D. Antonik, N. P. D'Costa, S. Nageswaran, C.-A. Schoenenberger, and J. H. Hoh, Relative microelastic mapping of living cells by atomic force microscopy, Biophys. J. **74**, 1564 (1998).

[14] P. A. Janmey, U. Euteneuer, P. Traub, and M. Schliwa, Viscoelastic properties of vimentin compared with other filamentous biopolymer networks, J. Cell Biol. **113**, 155 (1991).

[15] P. Pawelzyk, H. Herrmann, and N. Willenbacher, Mechanics of intermediate filament networks assembled from keratins K8 and K18, Soft Matter **9**, 8871 (2013).

[16] Y.-C. Lin, N. Y. Yao, C. P. Broedersz, H. Herrmann, F. C. MacKintosh, and D. A. Weitz, Origins of elasticity in intermediate filament networks, Phys. Rev. Lett. **104**, 058101 (2010).

[17] S. Zafari, S. Schirra, R. Mendozza, S. Lambert, K. A. T. Pajanonot, P. Kumari, P. Sollich, and S. Köster, Vimentin networks at high strains, Phys. Rev. Res. **8**, 013020 (2026).

[18] J. Block, H. Witt, A. Candelli, E. J. G. Peterman, G. J. L. Wuite, A. Janshoff, and S. Köster, Nonlinear loading-rate-dependent force response of individual vimentin intermediate filaments to applied strain, Phys. Rev. Lett. **118**, 048101 (2017).

[19] C. Lorenz, J. Forsting, A. V. Schepers, J. Kraxner, S. Bauch, H. Witt, S. Klumpp, and S. Köster, Lateral subunit coupling determines intermediate filament mechanics, Phys. Rev. Lett. **123**, 188102 (2019).

[20] C. Lorenz, J. Forsting, R. W. Style, S. Klumpp, and S. Köster, Keratin filament mechanics and energy dissipation are determined by metal-like plasticity, Matter **6**, P2019 (2023).

[21] L. Kreplak, H. Bär, J. F. Leterrier, H. Herrmann, and U. Aebi, Exploring the mechanical behavior of single intermediate filaments, J. Mol. Biol. **354**, 569 (2005).

[22] Z. Qin, L. Kreplak, and M. J. Buehler, Hierarchical structure controls nanomechanical properties of vimentin intermediate filaments, PLoS One **4**, e7294 (2009).

[23] N. Wang, J. P. Butler, and D. E. Ingber, Mechanotransduction across the cell surface and through the cytoskeleton, Science **260**, 1124 (1993).

[24] N. Wang and D. Stamenovic, Mechanics of vimentin intermediate filaments, J. Muscle Res. Cell Motil. **23**, 535 (2002).
[25] D. Fudge, D. Russell, D. Beriault, W. Moore, E. B. Lane, and A. W. Vogl, The intermediate filament network in cultured human keratinocytes is remarkably extensible and resilient, PLoS One **3**, e2327 (2008).
[26] K. Pogoda, F. Byfield, P. Deptuła, M. Cieśluk, L. Suprewicz, K. Skłodowski, J. L. Shivers, A. van Oosten, K. Cruz, E. Tarasovetc, E. L. Grishchuk, F. C. Mackintosh, R. Bucki, A. E. Patteson, and P. A. Janmey, Unique role of vimentin networks in compression stiffening of cells and protection of nuclei from compressive stress, Nano Lett. **22**, 4725 (2022).
[27] X. Trepat, L. Deng, S. S. An, D. Navajas, D. J. Tschumperlin, W. T. Gerthoffer, J. P. Butler, and J. J. Fredberg, Universal physical responses to stretch in the living cell, Nature (London) **447**, 592 (2007).
[28] I. Constantinou and E. E. Bastounis, Cell-stretching devices: Advances and challenges in biomedical research and live-cell imaging, Trends Biotechnol. **41**, 939 (2023).
[29] J. F. E. Bodenschatz, K. Ajmail, M. Skamrahl, M. Vache, J. Gottwald, S. Nehls, and A. Janshoff, Epithelial cells sacrifice excess area to preserve fluidity in response to external mechanical stress, Commun. Biol. **5**, 855 (2022).
[30] S. Nageswaran, J. Haipeter, J. F. E. Bodenschatz, R. Meyer, S. Köster, and C. Steinem, Membrane-bound vimentin filaments reorganize and elongate under strain, Biomacromolecules **24**, 2512 (2023).
[31] U. Faust, N. Hampe, W. Rubner, N. Kirchgeßner, S. Safran, B. Hoffmann, and R. Merkel, Cyclic stress at mHz frequencies aligns fibroblasts in direction of zero strain, PLoS One **6**, e28963 (2011).
[32] S. Massou, F. Nunes Vicente, F. Wetzel, A. Mehidi, D. Strehle, C. Leduc, R. Voituriez, O. Rossier, P. Nassoy, and G. Giannone, Cell stretching is amplified by active actin remodelling to deform and recruit proteins in mechanosensitive structures, Nat. Cell Biol. **22**, 1011 (2020).
[33] I. Andreu, B. Falcones, S. Hurst, N. Chahare, X. Quiroga, A.-L. Le Roux, Z. Kechagia, A. E. M. Beedle, A. Elosegui-Artola, X. Trepat, R. Farré, T. Betz, I. Almendros, and P. Roca-Cusachs, The force loading rate drives cell mechanosensing through both reinforcement and cytoskeletal softening, Nat. Commun. **12**, 4229 (2021).
[34] X. Trepat, M. Grabulosa, F. Puig, G. N. Maksym, D. Navajas, and R. Farré, Viscoelasticity of human alveolar epithelial cells subjected to stretch, Am. J. Physiol. Lung Cell. Mol. Physiol. **287**, L1025 (2004).
[35] S. Schürmann, S. Wagner, S. Herlitze, C. Fischer, S. Gumbrecht, A. Wirth-Hücking, G. Prölß, L. Lautscham, B. Fabry, W. Goldmann, V. Nikolova-Krstevski, B. Martinac, and O. Friedrich, The IsoStretcher: An isotropic cell stretch device to study mechanical biosensor pathways in living cells, Biosens. Bioelectron. **81**, 363 (2016).
[36] J. Duque, A. Bonfanti, J. Fouchard, L. Baldauf, S. R. Azenha, E. Ferber, A. Harris, E. H. Barriga, A. J. Kabla, and G. Charras, Rupture strength of living cell monolayers, Nat. Mater. **23**, 1563 (2024).
[37] N. Desprat, A. Richert, J. Simeon, and A. Asnacios, Creep function of a single living cell, Biophys. J. **88**, 2224 (2005).
[38] E. Latorre, S. Kale, L. Casares, M. Gómez-González, M. Uroz, L. Valon, R. V. Nair, E. Garreta, N. Montserrat, A. del Campo, B. Ladoux, M. Arroyo, and X. Trepat, Active superelasticity in three-dimensional epithelia of controlled shape, Nature (London) **563**, 203 (2018).
[39] See Supplemental Material at http://link.aps.org/supplemental/10.1103/s24m-n8wc for additional figures and movies.
[40] S. D. Poisson, *Traité de Mécanique* (Courcier, Paris, 1811).
[41] L. D. Landau and E. M. Lifshitz, *Theory of Elasticity*, 3rd ed., Course of Theoretical Physics No. 7 (Elsevier, Amsterdam, 2009).
[42] L. Galarneau, A. Loranger, S. Gilbert, and N. Marceau, Keratins modulate hepatic cell adhesion, size and G1/S transition, Exp. Cell Res. **313**, 179 (2007).
[43] A. Quaglino, M. Salierno, J. Pellegrotti, N. Rubinstein, and E. C. Kordon, Mechanical strain induces involution-associated events in mammary epithelial cells, BMC Cell Biol. **10**, 55 (2009).
[44] X. Trepat, F. Puig, N. Gavara, J. J. Fredberg, R. Farre, and D. Navajas, Effect of stretch on structural integrity and micromechanics of human alveolar epithelial cell monolayers exposed to thrombin, Am. J. Physiol. Lung Cell. Mol. Physiol. **290**, L1104 (2006).
[45] N. Gavara, A beginner's guide to atomic force microscopy probing for cell mechanics, Microsc. Res. Tech. **80**, 75 (2017).
[46] B. R. Brückner, H. Nöding, and A. Janshoff, Viscoelastic properties of confluent MDCK II cells obtained from force cycle experiments, Biophys. J. **112**, 724 (2017).
[47] E. K. Dimitriadis, F. Horkay, J. Maresca, B. Kachar, and R. S. Chadwick, Determination of elastic moduli of thin layers of soft material using the atomic force microscope, Biophys. J. **82**, 2798 (2002).
[48] A. Cordes, H. Witt, A. Gallemí-Pérez, B. Brückner, F. Grimm, M. Vache, T. Oswald, J. Bodenschatz, D. Flormann, F. Lautenschläger, M. Tarantola, and A. Janshoff, Prestress and area compressibility of actin cortices determine the viscoelastic response of living cells, Phys. Rev. Lett. **125**, 068101 (2020).
[49] P. Nietmann, J. E. Bodenschatz, A. M. Cordes, J. Gottwald, H. Rother-Nöding, T. Oswald, and A. Janshoff, Epithelial cells fluidize upon adhesion but display mechanical homeostasis in the adherent state, Biophys. J. **121**, 361 (2022).
[50] P. Chugh, A. G. Clark, M. B. Smith, D. A. D. Cassani, K. Dierkes, A. Ragab, P. P. Roux, G. Charras, G. Salbreux, and E. K. Paluch, Actin cortex architecture regulates cell surface tension, Nat. Cell Biol. **19**, 689 (2017).
[51] A. Pietuch, B. R. Brückner, T. Fine, I. Mey, and A. Janshoff, Elastic properties of cells in the context of confluent cell monolayers: Impact of tension and surface area regulation, Soft Matter **9**, 11490 (2013).
[52] G. Salbreux, G. Charras, and E. Paluch, Actin cortex mechanics and cellular morphogenesis, Trends Cell Biol. **22**, 536 (2012).
[53] S. Sen, S. Subramanian, and D. E. Discher, Indentation and adhesive probing of a cell membrane with AFM: Theoretical model and experiments, Biophys. J. **89**, 3203 (2005).
[54] G. A. C. Graham, The correspondence principle of linear viscoelasticity theory for mixed boundary value problems involving time-dependent boundary regions, Q. Appl. Math. **26**, 167 (1968).
[55] S. Karsch, F. Büchau, T. M. Magin, and A. Janshoff, An intact keratin network is crucial for mechanical integrity and barrier function in keratinocyte cell sheets, Cell. Mol. Life Sci. **77**, 4397 (2020).

[56] S. Nehls, H. Nöding, S. Karsch, F. Ries, and A. Janshoff, Stiffness of MDCK II cells depends on confluency and cell size, Biophys. J. **116**, 2204 (2019).

[57] F. Sauer, S. Grosser, M. Shahryari, A. Hayn, J. Guo, J. Braun, S. Briest, B. Wolf, B. Aktas, L. Horn, I. Sack, and J. A. Käs, Changes in tissue fluidity predict tumor aggressiveness in vivo, Adv. Sci. **10**, 2303523 (2023).

[58] R. M. Sarate, J. Hochstetter, M. Valet, A. Hallou, Y. Song, N. Bansaccal, M. Ligare, M. Aragona, D. Engelman, A. Bauduin, O. Campàs, B. D. Simons, and C. Blanpain, Dynamic regulation of tissue fluidity controls skin repair during wound healing, Cell **187**, 5298 (2024).

[59] M. W. Tibbitt and K. S. Anseth, Hydrogels as extracellular matrix mimics for 3D cell culture, Biotechnol. Bioeng. **103**, 655 (2009).

[60] D. M. Bryant, A. Datta, A. E. Rodríguez-Fraticelli, J. Peränen, F. Martín-Belmonte, and K. E. Mostov, A molecular network for de novo generation of the apical surface and lumen, Nat. Cell Biol. **12**, 1035 (2010).

[61] X. Wang, Q. Zhao, L. Wang, J. Liu, H. Pu, S. Xie, C. Ru, and Y. Sun, Effect of cell inner pressure on deposition volume in microinjection, Langmuir **34**, 10287 (2018).

[62] A. Perez-Tirado, U. Unkelbach, T. A. Oswald, J. Rheinlaender, T. E. Schäffer, M. Mukenhirn, A. Honigmann, and A. Janshoff, Differences in apical and basal mechanics regulate compliance of curved epithelia, Cell Rep. Phys. Sci. **6**, 102485 (2025).

[63] P. A. Galie, P. C. Georges, and P. A. Janmey, How do cells stiffen? Biochem. J. **479**, 1825 (2022).

[64] A. Cartagena-Rivera, J. Logue, C. Waterman, and R. Chadwick, Actomyosin cortical mechanical properties in nonadherent cells determined by atomic force microscopy, Biophys. J. **110**, 2528 (2016).

[65] R. Meyer, U. Unkelbach, P. Jain, U. Rölleke, N. Schwarz, A. Perez-Tirado, A. V. Schepers, C. Geisler, A. Janshoff, and S. Köster, Data for "The keratin cortex stabilizes cells and cell-cell contacts at high strains," https://doi.org/10.25625/MDCE31 (GRO.data, 2026).

[66] S. Deguchi, J. Hotta, S. Yokoyama, and T. S. Matsui, Viscoelastic and optical properties of four different PDMS polymers, J. Micromec. Microeng. **25**, 097002 (2015).

[67] C. M. Cesa, N. Kirchgeßner, D. Mayer, U. S. Schwarz, B. Hoffmann, and R. Merkel, Micropatterned silicone elastomer substrates for high resolution analysis of cellular force patterns, Rev. Sci. Instrum. **78**, 034301 (2007).

[68] F. A. Ran, P. D. Hsu, J. Wright, V. Agarwala, D. A. Scott, and F. Zhang, Genome engineering using the CRISPR-Cas9 system, Nat. Protoc. **8**, 2281 (2013).

[69] S. Klein, M. Staring, K. Murphy, M. Viergever, and J. Pluim, elastix: A toolbox for intensity-based medical image registration, IEEE Trans. Med. Imaging **29**, 196 (2010).

[70] D. Shamonin, E. E. Bron, B. P. Lelieveldt, M. Smits, S. Klein, and M. Staring, Fast parallel image registration on CPU and GPU for diagnostic classification of Alzheimer's disease, Front. Neuroinf. **7**, 1 (2014).

[71] C. Stringer, T. Wang, M. Michaelos, and M. Pachitariu, Cellpose: A generalist algorithm for cellular segmentation, Nat. Methods **18**, 100 (2021).

[72] M. Pachitariu and C. Stringer, Cellpose 2.0: How to train your own model, Nat. Methods **19**, 1634 (2022).

[73] J. Schindelin, I. Arganda-Carreras, E. Frise, V. Kaynig, M. Longair, T. Pietzsch, S. Preibisch, C. Rueden, S. Saalfeld, B. Schmid, J.-Y. Tinevez, D. J. White, V. Hartenstein, K. Eliceiri, P. Tomancak, and A. Cardona, Fiji: An open-source platform for biological-image analysis, Nat. Methods **9**, 676 (2012).

[74] P. Müller, S. Abuhattum, S. Möllmert, E. Ulbricht, A. V. Taubenberger, and J. Guck, Nanite: Using machine learning to assess the quality of atomic force microscopy-enabled nanoindentation data, BMC Bioinf. **20**, 465 (2019).